PROFILING CHARGED PARTICLE BEAMS USING COHERENT ATOMIC MAGNETOMETRY

Nicolas DeStefano and Irina Novikova
Department of Physics, William & Mary, Williamsburg. VA 23185

We present a non-invasive approach to imaging charged particle beams that generates profiles in 1 (and eventually 3) dimensions by monitoring the electron beam's effect on the quantum state of a surrounding atomic vapor. As the charged particle beam propagates, a magnetic field is generated, and the atoms in the detection medium respond with shifts in their atomic states. Moreover, we can measure this atomic response by observing the polarization of a probe laser. Imaging the components of this laser's polarization via cameras, we successfully map the variations in the electron beam magnetic field and can extrapolate electron beam characteristics, such as its position, width, and current density. We also show the validity of derived electron beam quantities using a Faraday cup and electron-induced rubidium fluorescence. This approach to charged particle detection may have a broad range of applications in accelerator, plasma, and cosmic ray physics as a non-invasive solution to charged particle tracking.

Charged particles make up vital constituents of phenomena occuring in deep space, and allow insight into the complex mechanisms of exotic space objects through the study of cosmic ray particles and space plasmas. Information from these plasmas and particles can be used to determine electromagnetic field behavior of stellar objects. Cosmic rays are such particles originating from active galactic nuclei and supernovae, which is capable of accelerating the particle to multiple 10^{20} eV, which upon entering Earth's atmosphere, generates a particle beam "shower" which is detectable through large particle detector arrays such as the Pierre Augur Observatory[1] and the Telescope Array[2]. Space plasmas have great impact on understanding celestial objects, which can range as local as the magnetospheres of planets to interstellar mediums far away. Gaining any information, such as electromagnetic field behavior of either of these phenomenon, is therefore integral to define interstellar object behavior.

Quantum sensing is a rapidly expanding field, building various sensors capable of measuring extremely small quantities. Where classical sensors consider measure macroscopic properties of the detector, quantum sensors consider specific quantum states of an object as a basis of detection. These sensitivities are achievable by monitoring and manipulating these quantum states associated with the sensor, and through this quantum-based approach we can measure fundamental properties with heightened precision. In particular, atomic magnetometers have been improved to measure sub-femtotesla magnetic fields, capable of detecting neuron activity generated by the human brain[3].

Particle detectors derive beam properties using light-based signals, where optical readouts indicate the presence of charged particles. In it's earliest form, bubble chambers were used to reveal the trajectories of highly energetic particles that would ionize the detection medium and mark the particle trajectory with the resulting vapor[4]. However, the lack of a conversion to a purely electronic signal lead to improvements to the acquisition of ionization events in the detection medium.

A typical detector relies on the scattering of an incident energetic charged particle off of a constituent in the detection medium. When colliding the two species, the detection medium is excited to a highly energetic state, and upon relaxation, emits light in the form of radiation to be detected in the local region of the scattering event. In the case of a continuous particle beam, record of these scattering events will reveal particle beam density, position, and width. This source of signals rely on high scattering rates of incident charged particles with the detection medium and will, by definition, decrease the transmission of the incident particle beam. Thus the requirements of these methods is to use high particle beam density to maintain the particle beam beyond the detection medium and high particle beam energy to ionize the detection medium.

Detectors outside of ionization processes include those who directly interact with the particle beam. The most rudimentary example being the harp scanner, which scans a wire across the beam profile to record the total beam current deposited on the harp as a function of wire position. Some modern scanners involve high-powered lasers to record the scattering of photons off of the charged particles through Compton scattering processes[5,6]. These processes still alter the original electron beam's trajectory and results in overall loss in the transmission of the electron beam in the detection medium.

Particle detection technology can benefit from quantum sensors by detecting the electromagnetic fields generated by charged particles as they propagate. Extracting key characteristics of the charged particle beam without sacrificing beam transmission to scattering events allows detection in low beam current regimes. In the case of using sensitive atomic magnetometers, the atoms retain the information of a passing charged particle for a short period independent of beam energy. Therefore, using a vapor of atoms as a detection medium provides essential beam parameters for a wide range of beam energies and charge densities.

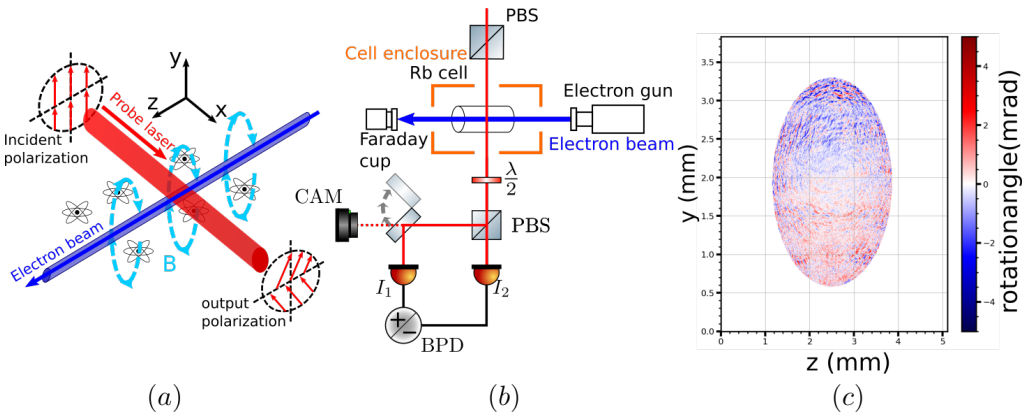

FIG. 1. (a) Conceptual schematic of the detection mechanism. When the beams are perfectly aligned to each other, the output polarization angle will rotate in opposite directions above and below the electron beam centroid. (b) Optical schematic of the atomic magnetometer. The cell enclosure includes a heated-air oven and magnetic shielding to preserve the sensitivity of the atomic response to electron beam magnetic field. A flipper mirror allows imaging of the polarization component and by rotating the $\lambda/2$ waveplate such that the polarization rotates 45 °, the opposite polarization component is imaged. (c) Experimental demonstration of the polarization rotation reversal for aligned laser and electron beams. The interface between positive and negative (red and blue) polarization rotation angle regions indicate the centroid position of the electron beam.

An electron beam generates a magnetic field as it propagates, perturbing the atomic spin states of the atoms in the detection medium. The shift of the atomic spin states can be observed through the output linear polarization angle of a resonant and coherent probe laser in Figure 1(a). Using the atoms as local probes for the electron beam's magnetic field, spatial gradients of the field are imaged and beam parameters such as position, width, and electron charge density are extracted. A unique feature of the electron beam's magnetic field is it's bi-directional behavior dependent on vertical position relative to the electron beam center. Therefore, a clear gradient will be captured when laser and charged particle beams are coincidently aligned, demonstrated in Figure 1(a).

The probe laser prepares the atomic state as a superposition of two seemingly identical (degenerate) ground states interacting with an excited state through the circular birefringence of a linearly polarized laser in Figure 2. When a magnetic field is induced perpendicular to the optical field's polarization, the ground states will shift by an amount in Equation 1 for δ the Zeeman energy level shift, μ_B the Bohr magneton, g the Lande g-factor, and B the magnitude of the magnetic field perpendicular to the optical field's polarization.

$$\delta_{\pm} = \pm \mu_B g B \tag{1}$$

These shifts will tune the resonances of the circular polarizations σ_- and σ_+ in Figure 2 such that the linear polarization angle of the optical field, a superposition of σ_- and σ_+, will rotate by angle ϕ. This interaction between magnetic field, atoms, and optical fields is referred to as nonlinear magneto-optical polarization rotation (NMOR), which has been used in a wide range of applications involving sensitive measurements to small magnetic fields[7–9].

The schematic for the detector is shown in Figure 1(b), where a tungsten hairpin electron source generates up to 200 μA current accelerated to 20 keV beam energy. The electron beam propagates through the glass cell containing the detection medium before terminating in the Faraday cup measuring the total current in the electron beam. The detection medium is made up of natural abundance ratio of ^{85}Rb (72%) and ^{87}Rb (28%) atoms at density 10^{12} atoms cm^{-3} interacting with a linearly polarized probe laser resonant to the D_2 transition of ^{85}Rb with

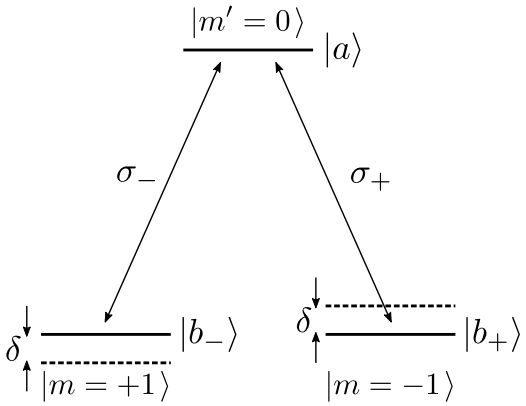

FIG. 2. Energy level diagram for nonlinear magneto-optical rotation, featuring the Λ scheme of two ground level atomic spin states $|b_-\rangle$ and $|b_+\rangle$ interacting with an excited state $|a\rangle$ through left- and right-handed circularly polarized optical fields σ_- and σ_+. In the presence of a magnetic field, the ground states shift by an amount δ linearly proportional to the magnetic field magnitude.

wavelength $\lambda = 780.241$ nm. Magnetic shielding encloses the detection cell heated to 60 °C by a heated-air oven for most optimal magnetometer sensitivity.

The linear polarization angle is calculated by considering both components that make up the linear polarization. Using a polarizing beam splitter (PBS) to resolve the two components of the optical field's linear polarization, we can analyze the total rotation and magnetic field through Equation 2 with ϕ the rotation angle of the linear polarization and $I_{1,2}$ the intensities of the corresponding PBS outputs.

$$\phi = \frac{1}{2}\frac{I_1 - I_2}{I_1 + I_2} \tag{2}$$

We can evaluate this rotation angle through a balanced photodetector (BPD) or a camera. The photodetector simultaneously evaluates the sum and difference of the polarization component's intensities, and by using photodiodes, the BPD boasts greater sensitivity to polarization rotation but lacks any spatial information of the magnetic field. The camera can image the total polarization rotation angle and can resolve gradients in the magnetic field causing the polarization rotation. The opposing linear polarization component is imaged by rotating the polarization input to the PBS 45° using the $\lambda/2$ waveplate in Figure 1(b). To ensure imaging of the electron beam magnetic field, the BPD is used to coarsely align the electron and laser beam until the opposing polarization rotation directions cancel out due to the unique form of the electron beam's magnetic field.

An example of imaging the polarization rotation angle after aligning the two beams is shown in Figure 1(c). The image shows distinct regions of positive and negative rotation angles, which correctly captures the electron beam magnetic field behavior: opposite in direction above and below the charged particle beam. When the electron beam is vertically translated, the interface between the positive and negative rotation shifts in the same direction, shown in Figure 3. In this series of images, the electron beam center corresponds to the interface between the two rotation angle hemispheres.

In order to reconstruct the current density of the charged particle beam from the polarization rotation angle, we model the electron beam as a distribution of infinitely thin wires. If we assume the polarization rotation is generated due to small magnetic fields then $d\phi = \beta(y,z)B_x dx$ for ϕ the rotation angle, $\beta(y,z)$ the atomic response to magnetic fields, B_x the magnetic field along the laser propagation path and dx the infinitesimal length along the laser propagation path[10]. Writing B_x in terms of the electron beam current density and assuming the length of the cell L is much larger than the electron beam, an expression for $\phi(y,z)$ in terms of the current density $j(y')$ results in equation 3. In the resulting integral, μ_0 is the vacuum permeability, D the camera sensor size, and $\mathrm{Sgn}(y-y')$ the signum function.

$$\begin{aligned}\phi(y,z) &= \frac{\mu_0\beta(y,z)}{2\pi}\int_{-\frac{D}{2}}^{\frac{D}{2}} j(y')dy' \int_{-\frac{L}{2}}^{\frac{L}{2}} \frac{(y-y')dx}{(y-y')^2+x^2} \\ &\approx \frac{\mu_0\beta(y,z)}{2}\int_{-\frac{D}{2}}^{\frac{D}{2}} j(y')\ \mathrm{Sgn}(y-y')dy' \end{aligned} \tag{3}$$

Inverting Equation 3 in terms of the current density integral and differentiating with respect to y yields an expression for the current density in the vertical direction in Equation 4. This result allows reconstruction of the electron beam density by differentiating the normalized rotation $\phi(y,z)/\beta(y,z)$ in the vertical direction.

$$j(y) = \frac{d}{dy}\left(\frac{\phi(y,z)}{\mu_0\beta(y,z)}\right) \tag{4}$$

In order to derive the atomic response coefficient $\beta(y,z)$ we recall the response of the polarization rotation angle to a magnetic field $d\phi(y,z) = \beta(y,z)B_x dx$. For a uniform magnetic field, the rotation is trivially solved by integrating along x through the length of the detection medium L and solving for the atomic coefficient resulting in Equation 5 for $\phi_0(y,z)$ and B_0 the polarization rotation and uniform magnetic field strength, respectively.

$$\beta(y,z) = \frac{\phi_0(y,z)}{B_0 L} \tag{5}$$

Normalizing the rotation to the atomic response and differentiating in the vertical direction using Equations 4 and 5 will result in the Gaussian electron beam current density profiles in Figure 4. By representing the profiles in terms of current density of the electron beam, we can derive essential beam parameters such as position, width, and total current through the fitting parameters and by integrating over the current density distribution.

In order to gauge the accuracy of derived beam parameters, we make use of the Faraday cup at the end of the beam path in Figure 1(b) and electron-induced rubidium fluorescence. The Faraday cup measures the total current and energy distribution of the charged particle beam, and consistently shows a loss of 30% beam transmission compared to the indicated emission current on the electron source controller. This loss of transmission is due to obstacles in the beam path as it propagates through the apparatus. The total current between the profiles in Figure 4 and the Faraday cup differ by less than 10%, with the polarization rotation detector falling within the 30% difference between Faraday cup and the electron source currents.

Electron-Induced rubidium fluorescence is a form of ionization based fluorescence, where electrons scatter off atoms in the vapor, exciting the atoms, and the atoms relax to their original ground state, emitting light in the process. Using this method, we can verify position and

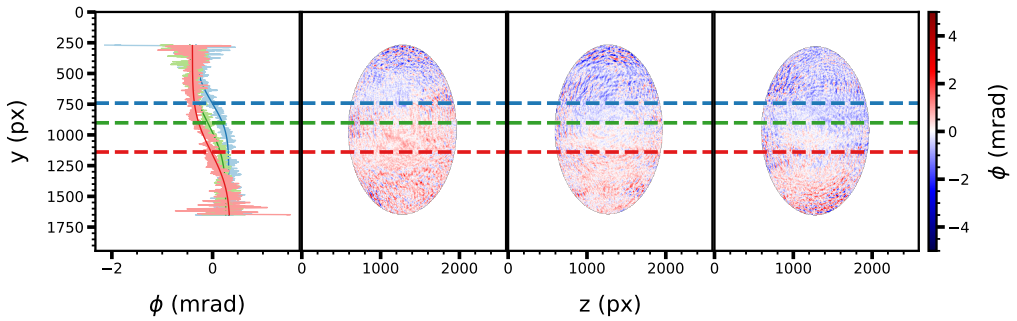

FIG. 3. Polarization rotation images for varied electron beam vertical positions. Shown left is the vertical projection of the images with overlaid error-function fits. The dashed lines are the parameters derived by fitting the image to an error function indicating where the center of the electron beam is located, coinciding with the interface between positive and negative rotation angles.

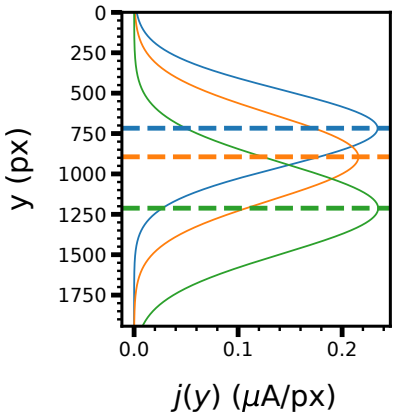

FIG. 4. Current density profiles for varied electron beam positions, obtained by differentiating the error-function fits in Figure 3. Overlaid is the identical centroid positions to track the movement of the electron beam. Integrating these current density profiles will yield the total current of the electron beam.

width quantities derived from the atomic magnetometer. To verify the positions, we track electron beam centroid position as a function of beam deflection voltage and compare the magnitude of the linear slopes between the two methods, where the magnitude is only considered due to the inversion of the vertical direction between the two imaging systems. When conparing the relative slopes to one another, a 12% difference is found, indicating high correlation between the two methods of electron beam position tracking. Currently though, we are troubleshooting a factor of 2 discrepancy in the widths of the electron beam, potentially due to the relative orientation between probe laser polarization to electron beam magnetic field.

While the electron beam parameters agree between the detection methods, the sensitivity still requires optimization, as the data shown uses 130-200 μA beam currents. An immediate solution would be to pulse the electron beam at greater than 100 Hz rates to reduce the technical low frequency noise, we can also exploit the quantum nature of coherent light to enhance sensitivity beyond the classical limit. Experiments have shown that using a squeezed light probe improves magnetometer sensitivity by 15%[11]. Magnetometer sensitivity can also be improved by more than 2 orders of magnitude by using a symmetry-breaking wave-mixing scheme[12].

We have shown that by using atomic magnetometers, we can detect the magnetic field of a continuous electron beam. Imaging the polarization rotation generated from the charged particle beam magnetic field correctly reveals the gradients, allowing tracking of the position of the electrons. Differentiating the normalized polarization rotation yields the current density distribution, deriving the particle beam width and total current. Comparing the total current and position to secondary measurements shows less than 12% difference, within the variance of the parameters over multiple identical polarization rotation datasets. As we refine the precision and accuracy of the prototype detector, we plan on replicating the setup for plasmas and relativistic electron beams as a non-invasive detector for a wide bandwidth of beam energies and current densities.

[1] I. Allekotte et al. The surface detector system of the pierre auger observatory. *Nuclear Instruments and Methods in Physics Research Section A: Accelerators, Spectrometers, Detectors and Associated Equipment*, 586(3):409–420, 2008.

[2] T. Abu-Zayyad et al. The surface detector array of the telescope array experiment. *Nuclear Instruments and Methods in Physics Research Section A: Accelerators, Spectrometers, Detectors and Associated Equipment*, 689:87–97, 2012.

[3] IK Kominis, TW Kornack, JC Allred, and Michael V Romalis. A subfemtotesla multichannel atomic magnetometer. *Nature*, 422(6932):596–599, 2003.

[4] WILLIAM B Fretter. Nuclear particle detection (cloud chambers and bubble chambers). *Annual Review of Nuclear Science*, 5(1):145–178, 1955.

[5] L. Corner, A. Aryshev, G.A. Blair, S.T. Boogert, P. Karataev, K. Kruchinin, L.J. Nevay, N. Terunuma, J. Urakawa, and R. Walczak. Laserwire: A high resolution non-invasive beam profiling diagnostic. *Nuclear Instruments and Methods in Physics Research Section A: Accelerators, Spectrometers, Detectors and Associated Equipment*, 740:226–228, 2014. Proceedings of the first European Advanced Accelerator Concepts Workshop 2013.

[6] T. Hofmann, G.E. Boorman, A. Bosco, S.M. Gibson, and F. Roncarolo. A low-power laserwire profile monitor for h- beams: Design and experimental results. *Nuclear Instruments and Methods in Physics Research Section A: Accelerators, Spectrometers, Detectors and Associated Equipment*, 903:140–146, 2018.

[7] D. Budker, W. Gawlik, D. F. Kimball, S. M. Rochester, V. V. Yashchuk, and A. Weis. Resonant nonlinear magneto-optical effects in atoms. *Rev. Mod. Phys.*, 74:1153–1201, Nov 2002.

[8] Antoine Weis, Georg Bison, and Zoran D. Grujić. Magnetic resonance based atomic magnetometers. In A. Grosz, M. Haji-Sheikh, and S. Mukhopadhyay, editors, *High Sensitivity Magnetometers. Smart Sensors, Measurement and Instrumentation*, volume 19, pages 361–424. Springer, Cham, 2017.

[9] Kai Mei C. Fu, Geoffrey Z. Iwata, Arne Wickenbrock, and Dmitry Budker. Sensitive magnetometry in challenging environments. *AVS Quantum Science*, 2(4):044702, 12 2020.

[10] Herbert Piller. Chapter 3 faraday rotation. volume 8 of *Semiconductors and Semimetals*, pages 103–179. Elsevier, 1972.

[11] Jiahui Li and Irina Novikova. Improving sensitivity of an amplitude-modulated magneto-optical atomic magnetometer using squeezed light. *Journal of the Optical Society of America B*, 39(11):2998, October 2022.

[12] Feng Zhou, Chengjie J. Zhu, Edward W. Hagley, and Lu Deng. Symmetry-breaking inelastic wave-mixing atomic magnetometry. *Science Advances*, 3(12):e1700422, 2017.